PHYSICAL REVIEW APPLIED **21,** 054006 (2024)

Vortex decomposition and reconfiguration via transformation optics

Zhibin Zhang,[1,§] Pengfei Zhao,[2,§] Junke Liao,[2] Mengwei Dai,[2] Jianyang Zhou,[1,*]
Wen Xiao,[2,3,†] and Huanyang Chen[2,3,‡]

[1] *Department of Microelectronics and Integrated Circuit, Xiamen University, Xiamen, Fujian, 361005, China*
[2] *Department of Physics, Xiamen University, Xiamen, Fujian, 361005, China*
[3] *Jiujiang Research Institute of Xiamen University, Jiujiang, Jiangxi, 332000, China*

(Received 14 December 2023; revised 16 March 2024; accepted 29 March 2024; published 2 May 2024)

The potential of optical orbital angular momentum (OAM) to create boundless dimensional Hilbert spaces has garnered considerable interest for augmenting the capacity of communication systems. Precise detection and reconfiguration of optical vortices (OVs) carrying distinct topological charges are crucial for leveraging their communicative potential. Here, based on transformation optics (TO), we theoretically propose a straightforward method for OV decomposition and reconfiguration. We first transform spiral vortices into planar waves with varying refraction angles and subsequently restore the vortices at designated image points with the aid of coherent perfect absorbers. Employing Hamiltonian optics, we analyze the trajectory of OV rays at both source and image positions, revealing an efficient reconfiguration of the OAM field that accounts for the phases of the sources. Our findings demonstrate flexible manipulation of OAM through TO, offering substantial advancements in communication technologies, including on-chip signal filtering and demultiplexing.

DOI: 10.1103/PhysRevApplied.21.054006

I. INTRODUCTION

Optical orbital angular momentum (OAM) [1,2] has been widely investigated in the last few years, playing a crucial role in a variety of fields, including plasmonics, quantum computing, and sensing [3–6], and showing fascinating physical characteristics with promising applications in optical tweezers, imaging, quantum entanglement, and communications [7–15]. In recent years, OAM has attracted growing interest for its potential in multiplexing degrees of freedom to improve signal capacity and transmission efficiency [16–18]. Expanding the signal bandwidth using OAM-carrying signals will be the dominant method for future communication technologies.

The conventional OAM beams used in communications mainly include Laguerre-Gaussian beams, Bessel beams, perfect optical vortices (OVs), and vector vortices [1,19–21], which are described as vortices with azimuthal-dependent phase dislocation $e^{il\theta}$ [l is the topological charge (TC) determined by the OAM quantum state, and θ is the azimuthal angle]. The OAMs of distinct channels are discriminated by different TCs l, which correspondingly generate diverse spiral phases [22,23]. The generation of OAM is the first step in multichannel multiplexing communications, providing a foundation for subsequent signal modulation and demodulation. Considerable research efforts have been devoted to exciting vortices based on their spiral phase, including spatial light modulators, metasurfaces, and microlasers [24–27]. The OAM currently employed in communications features a helical phase in the out-of-plane direction (z direction), and it is important to consider the impact of atmospheric turbulence [28]. Despite great success in exciting vortices, a bottleneck issue, not overcome in previous studies, is how to achieve long-distance propagation in the air. The OAM with an in-plane spiral phase, resembling a vortex, presents a promising alternative for communications. This approach represents a prospective solution for overcoming the challenges associated with atmospheric turbulence in long-distance OAM communications.

OVs with OAM are essentially electromagnetic waves, hence the general wave regulation theory can be utilized to manipulate OAM, such as through using metasurfaces and transformation optics (TO) [29,30]. TO proposes a method for designing media with the desired electromagnetic properties through coordinate transformation from virtual space to physical space. Various optical devices based on TO have been proposed, such as cloaks, rotators, and concentrators [31–33]. In particular, there has been interest in applying TO techniques to manipulate

---

[*] Corresponding author: zhoujy@xmu.edu.cn
[†] Corresponding author: 15162148216@163.com
[‡] Corresponding author: chymetric@gmail.com
[§] These authors contributed equally to this work

optical vortices. For instance, a negative radiation pressure can be generated by transforming OAM to achieve a long-range optical pulling force beam [34]. TO also allows us to control OAM, transforming it from directional to omnidirectional in the horizontal plane [35]. Additionally, there has been significant research dedicated to the generation of OAM using TO [36–38]. However, there has been limited research on the reconfiguration of OVs with the in-plane spiral phase, whether utilizing TO or metasurfaces. In this work, we use TO to decompose and reconfigure OVs with the in-plane spiral phase. Firstly, as depicted in Fig. 1(a), we decompose the vortices with different TCs into specific characteristic plane waves. The spiral phases of OVs are interpreted into varying phases at each tangential point. Subsequently, in Fig. 1(b), we demonstrate internal-converged OV reconfiguration by the method of mirrored TO [39]. To reconfigure the OV, it is necessary to simultaneously map the phase from every azimuthal angle. Therefore, we arrange the media in a closed configuration to gather omnidirectional phases and visualize them with the help of a coherent perfect absorber (CPA). The efficient vortex decomposition and reconfiguration are theoretically and numerically validated. We analyze the unique spiral phase properties of OVs, contributing to the advancement of OAM-based communication techniques.

II. RESULTS AND DISCUSSION

Compared with a conventional cylindrical wave, the OV with an in-plane spiral phase carries an additional azimuthal phase induced by a nonzero TC l. When the propagating phase of the OV is canceled out, the azimuthal phase does not vanish, which might provide us with a method to identify the OAM of the TC. Following this approach, we can design an OV decomposer using TO, as shown in Fig. 1(a) This decomposer is created by compressing a fan shape air domain, and making the corresponding coordinate transformation as follows:

$$r' = \frac{h}{R_0\cos\theta - a}(r - R_0) + \frac{a+h}{\cos\theta}, \quad \theta' = \theta, \quad z' = z,$$
$$\text{for} \quad \frac{a}{\cos\theta} < r < R_0, \ -\theta_0 < \theta < \theta_0. \tag{1}$$

By keeping the θ unchanged, the arc-shaped emission boundary [virtual space in Fig. 1(c)] is compressed into the straight-line boundary [physical space in Fig. 1(d)]. From TO, the electromagnetic properties of the decomposer in Cartesian coordinates are

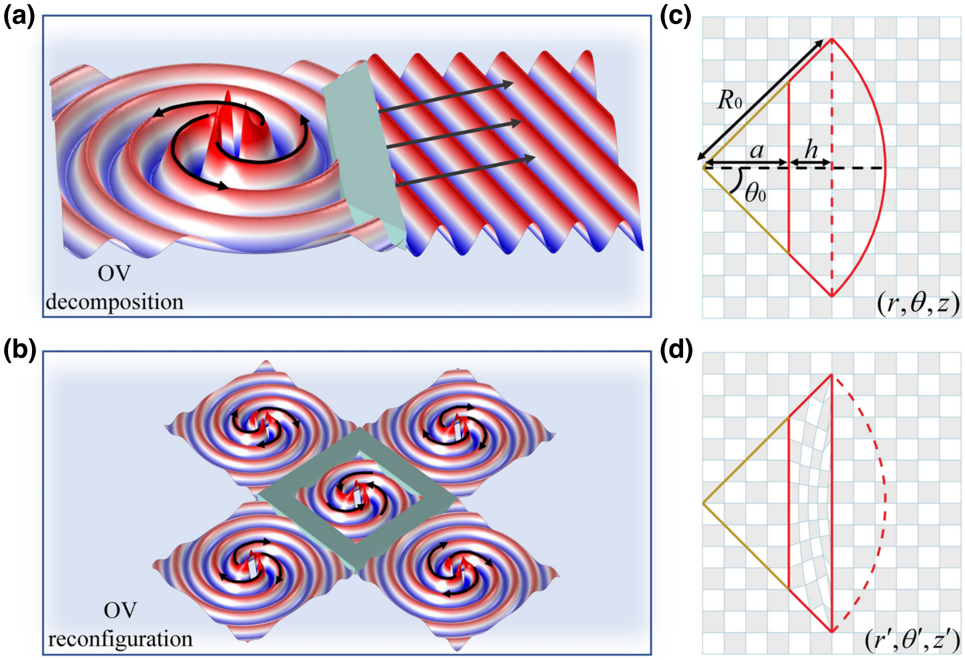

FIG. 1. Schematic of OV decomposition (a) and reconfiguration (b) through transformation optics. (c) A sector region bound by red solid lines in virtual space. The right boundary is $r = R_0$ ($|\theta| \leq \theta_0$) and the left one is $r\cos(\theta) = a$. The space is represented by a black and white rectangular grid referring to the unity refractive index. (d) A trapezoid region bounded by red solid lines in physical space with a thickness of h. The background grid is compressed to represent transformation and the induced inhomogeneous permittivity and permeability.

$$\overset{\leftrightarrow}{\varepsilon}=\overset{\leftrightarrow}{\mu}=\begin{pmatrix}\cos\theta' & -\sin\theta' & 0\\ \sin\theta' & \cos\theta' & 0\\ 0 & 0 & 1\end{pmatrix}\begin{pmatrix}-\dfrac{C}{Ar'}-\dfrac{D^2}{ACr'\cos^2\theta'}\tan^2\theta' & -\dfrac{D\tan\theta'}{C\cos\theta'} & 0\\ -\dfrac{D\tan\theta'}{C\cos\theta'} & -\dfrac{r'A}{C} & 0\\ 0 & 0 & -\dfrac{AC}{h^2r'}\end{pmatrix}\begin{pmatrix}\cos\theta' & \sin\theta' & 0\\ -\sin\theta' & \cos\theta' & 0\\ 0 & 0 & 1\end{pmatrix}, \tag{2}$$

where $r'=\sqrt{x^2+y^2}$, $\theta'=\arctan(y/x)$, $A=a-R_0\cos\theta'$, $B=r'-(a+h/\cos\theta')$, $C=hR_0-AB$, $D=a(a+h)-r'R_0\cos^2\theta'$. The values of a and h can be adjusted accordingly on demand. Here, we set $a=2\lambda$, $h=\lambda$, and $\theta_0=\pi/4$, where λ is the working wavelength in air. It is evident that the trajectories of light in the OV decomposer are refracted, and light rays will propagate at an angle depending on the TC l. We use the Hamiltonian optics [40] method to vividly show the manipulation of rays, and the Hamiltonian is written as follows:

$$H=knk-\det(n), \tag{3}$$

where k is the wave vector of the light, and n is the permittivity (or permeability). The results of ray trajectories are shown in Fig. 2, and the gray area is the decomposer. It can be found that the light is emitted perpendicular to the right boundary when $l=0$ in Fig. 2(c), which is consistent with our analysis. The vanishing OV means no additional azimuthal phase; thus, the right boundary is the equiphase plane. As l decreases (or increases), the phase on the right boundary is changed, such that light is emitted from the interface at different angles, such as in Fig. 2(a) for $l=-3$ and Fig. 2(e) for $l=3$. In the numerical calculations, the red solid circle in Figs. 2(a) and 2(e) represents the OV source, and the rays are emitted in a tangential direction to the circle. The different OV orders can be achieved by adjusting radius of red solid circle and distribution of tangential lines [41]. As an example, we depict the field pattern at 0.3 GHz for a point source set near the decomposer, as shown in Figs. 2(b), 2(d), and 2(f), and choose transverse electric polarization in this article. All the calculations in this article are performed by the commercial software COMSOL Multiphysics. After passing through the decomposer, the original cylindrical wave evolves into a tilted plane wave. Importantly, the tilted angle (or refraction angle) can be solved analytically.

Wave compression using TO usually leads to phase mismatch and significant deflection of light. Here, through our meticulous design, only a slight deflection is observed on the left side, and it only affects the right side. The phase in the right boundary varies along the y direction because of the additional azimuthal phase carried by the OV in

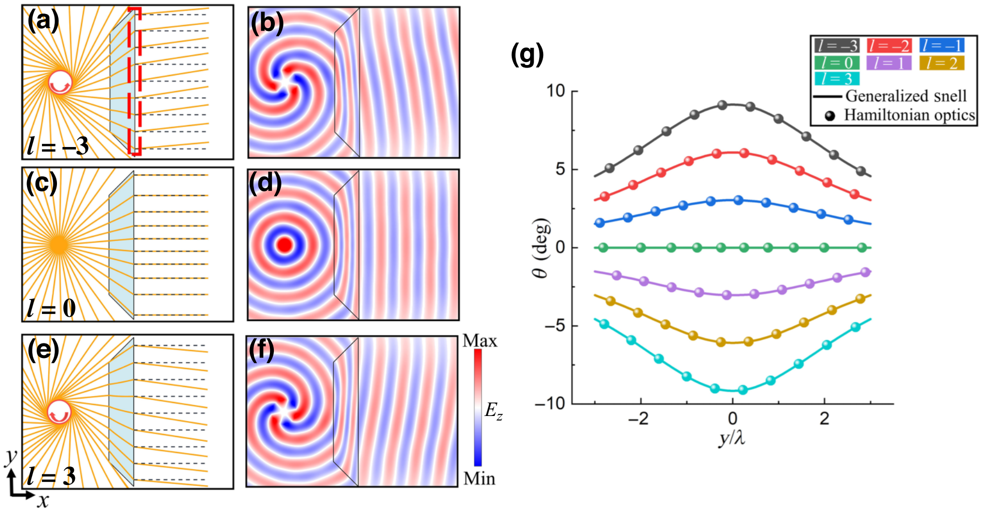

FIG. 2. Optical vortex (OV) decomposition. The Hamiltonian optics analysis for (a) $l=-3$, (c) $l=0$, (e) $l=3$. OV rays from a circle emit diagonally, while the point source emits vertically. Yellow lines are the trajectories of light rays, the gray area is the medium, black dashed lines indicate the vertical direction of the boundary, and red arrows indicate the exit spirality of the light. The simulated electric field patterns for (b) $l=-3$, (d) $l=0$, (f) $l=3$. The trapezoid region bounded by black solid lines is the medium. (g) The relationship between refraction angle and emission position [as depicted by the red dashed box in (a)] for different modes.

virtual space, which can be described as

$$\phi(y) = l\theta = l\arctan\left(\frac{y}{a+h}\right). \tag{4}$$

According to the generalized Snell's law [25], the refractive angle can be deduced as follows:

$$\alpha = \arcsin\left(\frac{l\lambda}{2\pi}\frac{d\phi(y)}{dy}\right). \tag{5}$$

By combining Eqs. (4) and (5), the refractive angle of rays is given as follows:

$$\alpha = \arcsin\left(\frac{l\lambda}{2\pi}\frac{a+h}{(a+h)^2+y^2}\right). \tag{6}$$

To validate Eq. (6), we compare the results calculated by Hamiltonian optics (lines) with the theoretical y-dependent α governed by Eq. (6) (dots) in Fig. 2(g), which show good agreement with each other. Light of OVs with different TCs produces different refraction angles after passing through the medium, and when $l < 0$, the light refracts upward, while it refracts downward when $l > 0$.

To reconfigure the OV, we need to construct the spiral phase surface of the OV, as depicted in Fig. 1(b). In the previous discussion, we demonstrate that the OV corresponds to a plane wave that is emitted obliquely. According to the principle of reversibility of light paths, when an oblique incident plane wave strikes the other side of the medium, it will generate part of the OV. However, during the transformation process, where the output surface is compressed, phase mismatch occurs between the output surface and the environment. This phase mismatch causes reflections when a plane wave is excited from the right side. To overcome this issue, we employ mirrored TO for phase matching, which uses a bilayer transformation medium as depicted in Fig. 3(a), and the mirrored transformation of medium II is as follows:

$$x' = 2(a+h) - x, y' = -y, z' = z. \tag{7}$$

According to mirrored TO, the incident source will form an image point at a symmetric position as shown in Fig. 3(a). First, we trace the light rays based on Hamiltonian optics, as depicted in Figs. 3(b)–3(d). When $l = 0$ [Fig. 3(c)], the initially divergent light rays converge to a point. When $l \neq 0$, the light rays emitted at a tangent to the circle return to the tangent trajectory of the circle at a symmetric position and produce a corresponding offset in the y direction. For $l < 0$, the light rays from the lower half space converge upward, while for $l > 0$, the light rays from the upper half space converge downward. We also conduct wave simulations, as illustrated in Figs. 3(e)–3(g). After passing through the bilayer transformation medium, vortices with different TCs are focused on distinct points. The black dashed line indicates the horizontal position of the source. When $l = 0$, the focus and source are on the same horizontal plane. For $l < 0$, the focus is above the horizontal line, and for $l > 0$, it is below the horizontal line. These results are consistent with those analyzed by Hamiltonian optics.

The direction of deflection is opposite to the vortex Hall effect [42] in double-negative refractive index materials. The image and corresponding source are mirror-symmetric within double negative refractive index materials, while they are rotationally symmetric in our design. When a cylindrical wave is incident, no Hall effect occurs, and instead it converges at the symmetric focal points. As discussed in the beginning of this section, a vortex is a cylindrical wave with an additional phase. It is precisely this additional phase that gives rise to these vortex Hall effects.

Despite the mirrored TO, waves emitted from a point source cannot be reconfigured to the same point source at a symmetrical position, but produce a light spot. Combining

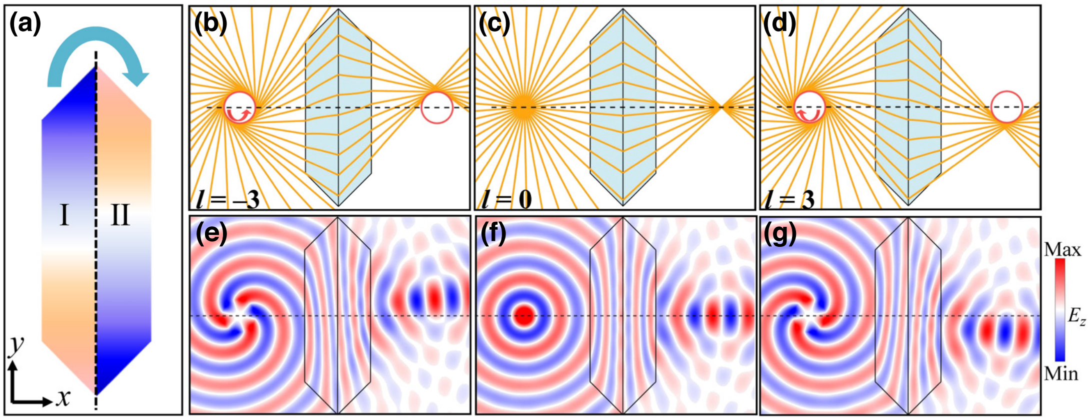

FIG. 3. Imperfect OV reconfiguration. (a) Schematic diagram of mirrored TO. (b)–(d) Hamiltonian optics analysis for $l = -3$, 0, 3, respectively. The black dashed line indicates center of the source. (e)–(g) Simulated electric field distributions for $l = -3$, 0, 3.

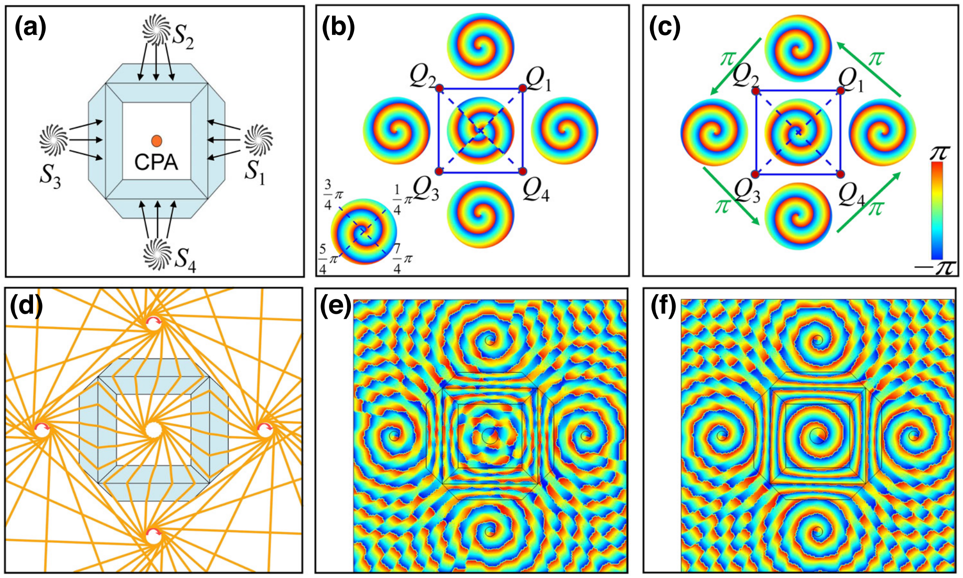

FIG. 4. Perfect OV reconfiguration. (a) Schematic diagram of OV reconfiguration, where CPA is a coherent perfect absorber. S_1, S_2, S_3, and S_4 represent four vortex sources around device. (b) OV phase discontinuity. (c) Phase continuity. Q_1, Q_2, Q_3, and Q_4 represent four corners of the device. (d) Hamiltonian optics analysis yields the results of OV reconfiguration. Simulation results of phase distribution in the case of (e) discontinuity and (f) continuity.

the results of Hamiltonian optics, it can be inferred that the medium has a limited ability to collect rays within a specific range of angles ($2\theta_0$), causing the formation of a refraction caustic with a half circle and resulting in an inability to reconfigure the OV. In order to reconfigure the OV, omnidirectional rays must be collected in geometric optics and, for waves, the phases at all angles (360°) must be gathered. As shown in Fig. 4(a), the medium in Fig. 3(a) is spliced and rotated to form a quadrilateral shape. Four OV sources are symmetrically positioned at a distance of $d = 2\lambda$ from the device's edge to generate the phase of each part. The medium gathers the omnidirectional phase required to reconfigure the OV.

Next, we employ Hamiltonian optics to calculate the trajectories of light rays, as depicted in Fig. 4(d). The converging surrounding light rays form a image of equal size at the center, showcasing the potential for OV reconfiguration. However, in wave optics, this image can not be reconfigured by simply placing identical OVs around the device. In the case of a quadrilateral shape, the designed medium must collect certain fragments of phase information from each source to reconfigure the OV. Given that the size of the medium has little impact on the results, we can simplify it as a slice or even a straight line, as illustrated in Fig. 4(b), when analyzing the phase. As the wave front of the OV is not circular but spiral, this leads to specific phase values at each azimuth angle [as shown in the inset in Fig. 4(b)]. The phase distribution of the spiral phase introduced by the surrounding sources (with $l = 1$) is presented in Table I.

At the boundary between each medium, a phase jump occurs, causing discontinuous phases, as illustrated in Fig. 4(b) and the simulated phase distribution in Fig. 4(e). To ensure continuous phases, the reconfigured phases must be consistent between the adjacent media. Therefore, a certain initial phase must be introduced between the neighboring sources. For an n-sided polygonal splice, the additional initial phase for the ith source is $\Delta\theta_i = -(4\pi/n)i$. For quadrilateral splicing, the phase difference between the sources is $\Delta\theta = -\pi$, as shown in Fig. 4(c). After assigning the appropriate initial phases to each respective source, a continuous converged phase is obtained at the center. It can be clearly observed that the spiral phase of the OV can be reconfigured at the center of the quadrilateral, as demonstrated by the simulated phase distribution presented in Fig. 4(f).

To investigate the generality of OV reconfiguration, different polygons are spliced by changing the angle $2\theta_0$ in

TABLE I. The phase distribution projected onto the center.

Position	Phase
$Q_1 \rightarrow Q_4$	$\frac{3}{4}\pi \rightarrow \frac{5}{4}\pi$
$Q_4 \rightarrow Q_3$	$\frac{1}{4}\pi \rightarrow \frac{3}{4}\pi$
$Q_3 \rightarrow Q_2$	$\frac{7}{4}\pi \rightarrow \frac{1}{4}\pi$
$Q_2 \rightarrow Q_1$	$\frac{5}{4}\pi \rightarrow \frac{7}{4}\pi$

TABLE II. The electromagnetic parameters corresponding to various TCs when the radius is set to 0.5λ.

TC	n_{CM}	α
0	0.9877	0.5487π
1	0.2661	0.5552π
2	0.5485	0.5830π
3	0.8915	0.6718π
4	1.1511	0.8653π
5	1.1335	0.9774π

virtual space and the corresponding number of vortices with initial phases is excited to reconfigure the vortices. Energy converges towards the center from all directions, resulting in interference that prevents effective reconfiguration of vortices. In practical applications, a receiving port is typically used to gather signals from all directions without mutual interference. To simulate this scenario, a CPA [43,44] is placed at the center to absorb energy from all directions. A CPA is an infinite conjugate metamaterial cylinder, and its electromagnetic parameters are given as $\varepsilon = n_{\mathrm{CM}}\exp(i\alpha)$, $\mu = n_{\mathrm{CM}} exp(-i\alpha)$, where n_{CM} and α, are the amplitude and phase factor of the conjugate metamaterial (CM), respectively. The values of n_{CM} are intricately tied to the radial size of the CPA. Here, we set the radius of the CPA to be 0.5λ, and the corresponding n_{CM} values are presented in Table II.

We showcase the results of OV reconfiguration with $l = 1,2,3$ for triangular, quadrilateral, and pentagonal patterns in Figs. 5(a)–5(c). The OV can be reconfigured at the center regardless of the number of sides on the polygon, as shown in Video 1, illustrating the wave propagation process. However, compared with triangles, pentagons exhibit results that are less effective due to the increased proximity of sources that leads to interference between them and consequently produces suboptimal performance at the center.

Next, let us discuss the realization and material parameters of this design. The materials predominantly used in TO are mostly unattainable in nature and can only be realized through metamaterials [45–48]. The electromagnetic parameters presented by Eq. (2) are challenging to implement owing to the inclusion of nondiagonal elements, but a mitigated version of the effects can be achieved by reducing the electromagnetic parameters [31,48]. The electromagnetic parameters in the article can be reduced through diagonalization to remove nondiagonal elements. The reduced electromagnetic parameters are as follows:

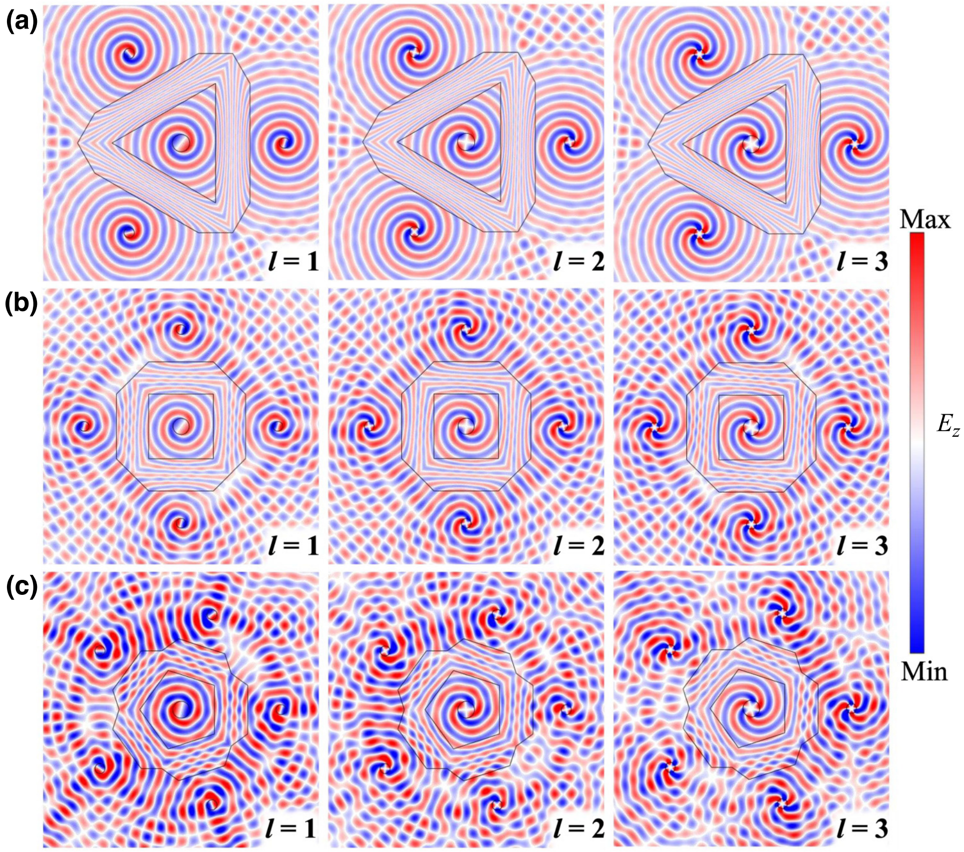

FIG. 5. OV reconfiguration in different scenarios: (a) triangle, (b) quadrilateral; (c) pentagon. The left, middle and right columns represent the situations when $l = 1, 2, 3$, respectively.

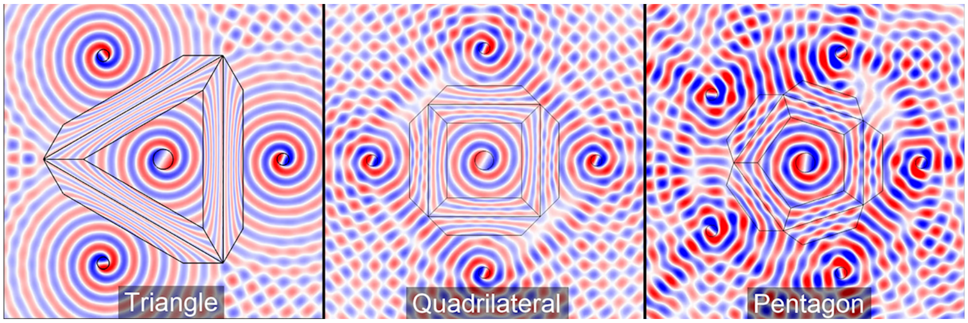

VIDEO 1. Visualization of the OV reconfiguration with triangle, quadrilateral and pentagon.

$$\overleftrightarrow{\varepsilon} = \overleftrightarrow{\mu} = \begin{pmatrix} \begin{array}{c} -\dfrac{C}{Ar}\cos^2\theta - \dfrac{D^2}{ACr}\tan^2\theta - \dfrac{rA}{C}\sin^2\theta \\ +2\dfrac{D}{C}\sin\theta\tan\theta \end{array} & 0 & 0 \\ 0 & \begin{array}{c} -\dfrac{C}{Ar}\sin^2\theta - \dfrac{D^2}{ACr}\tan^4\theta - \dfrac{rA}{C}\cos^2\theta \\ -2\dfrac{D}{C}\sin\theta\tan\theta \end{array} & 0 \\ 0 & 0 & -\dfrac{AC}{h^2 r} \end{pmatrix}.$$

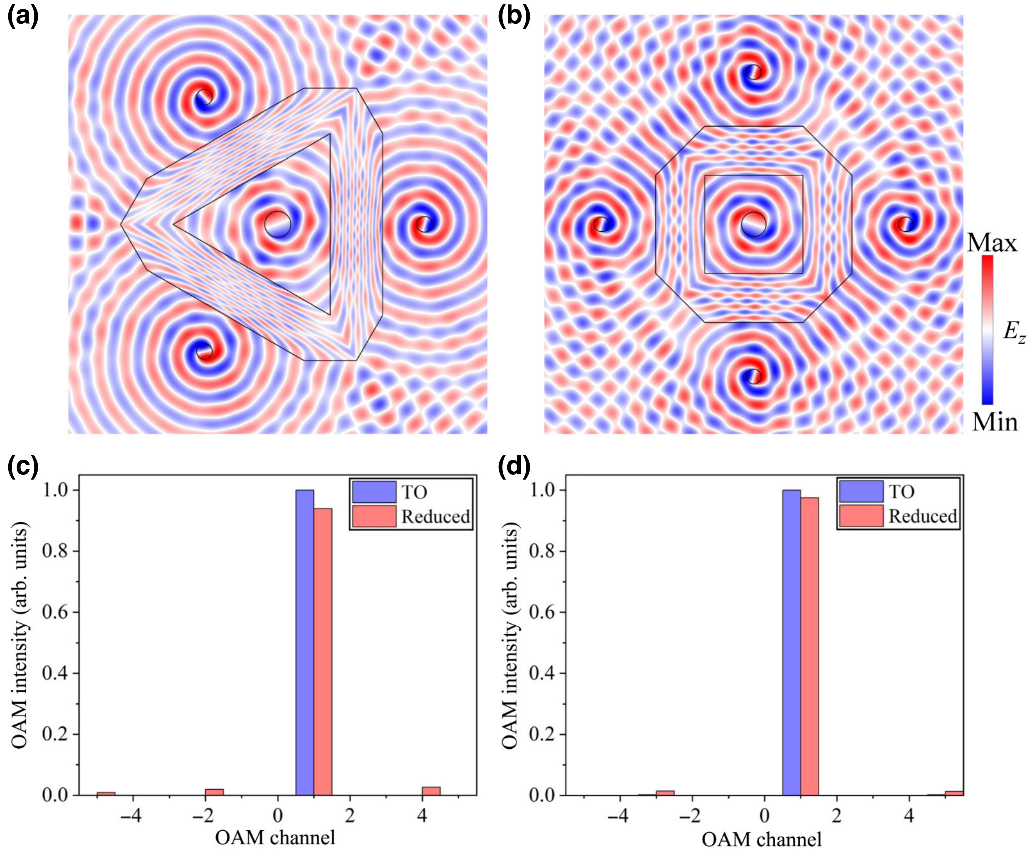

FIG. 6. OV reconfiguration with the reduced material properties. The fields shown are (a) triangle with $d = 1.8\lambda$; (b) quadrilateral with $d = 2.2\lambda$. The reconstructed OAM intensity spectra for the OV source excitation with $l = 1$ for (c) triangle and (d) quadrilateral.

The OV reconfiguration field obtained by splicing these materials is shown in Figs. 6(a) and 6(b). Compared with the nondiagonalized OV reconfiguration in Fig. 5, materials with reduced parameters can also achieve OV reconfiguration with patterns featuring some scattering. As shown in Figs. 6(c) and 6(d), we integrate the reconfigured field with OVs of different orders to obtain the intensity spectra of the reconfigured OVs, and they are normalized to the maximum component of TO. Whether in the case of a triangle or a square, the OV intensity spectrum is predominantly characterized by the component $l = 1$, in comparison to the parasitic ones both before and after reduction. This indicates that the reconfigured vortex primarily consists of an OV with $l = 1$.

III. CONCLUSION

In summary, we show that TO can be employed for OV decomposition and reconfiguration. By utilizing carefully designed transformation media, the properties of incident OVs can be manipulated, decomposed into different components, and reconfigured as desired. Hamiltonian optics analysis and simulation results demonstrate that vortices with distinct TCs can be decomposed into planar waves with varying refractive angles. The designed medium is folded using mirrored TO for phase matching and to achieve the results from the point source to the focal point. However, OVs cannot be reconfigured due to a lack of phase compensation. After analysis, it is discovered that OV reconfiguration requires the collection of phase information for each azimuth angle, and this collected information must be continuous. In our work, we splice designs of TO media to accomplish this task. TO transcends its application in optics and can be extended to various other physical fields, including acoustics, water waves, and elastic waves [49,50]. The decomposition and reconfiguration of vortices can yield comparable outcomes in acoustics.

In contrast to a prior study employing metagratings founded on phase discontinuities [51], our approach leverages TO to realize oblique plane waves as dictated by TCs. The physics behind the concepts of phase discontinuities and transformation optics are indeed different. The former refers to abrupt changes in the phase of an electromagnetic field across a surface or interface. These phase jumps can be utilized to manipulate and control the behavior of light, such as steering beams or creating OVs. Phase discontinuities are typically achieved through the design and implementation of metasurfaces or structured materials with carefully engineered properties. The latter is a mathematical framework that allows for the design of artificial media with desired electromagnetic properties. TO is based on the principles of coordinate transformation and involves modifying the spatial distribution of permittivity and permeability to achieve the desired transformation of light, such as bending or cloaking. Our approach not only offers alternative perspectives for applying OAM in other classical physical fields, like acoustics and water waves, but also provides additional insight into and exploration of the TO and phase discontinuities in metasurfaces and metagratings.

ACKNOWLEDGMENTS

Project supported by National Key Research and Development Program of China (Grants No. 2020YFA0710100, No. 2023YFA1407100); National Natural Science Foundation of China (Grants No. 12374410, No. 92050102); Jiangxi Provincial Natural Science Foundation (Grant No. 20224ACB201005); Fundamental Research Funds for the Central Universities (Grants No. 20720230102, No. 20720220033). We would like to thank Dr. Yangyang Zhou, Dr. Yuhang Yin, Dr. Shan Zhu, and Mr. Shanshan Jie for discussions about this paper.

[1] L. Allen, M. W. Beijersbergen, R. J. C. Spreeuw, and J. P. Woerdman, Orbital angular momentum of light and the transformation of Laguerre-Gaussian laser modes, Phys. Rev. A **45**, 8185 (1992).

[2] G. Molina-Terriza, J. P. Torres, and L. Torner, Twisted photons, Nat. Phys. **3**, 305 (2007).

[3] Seong-Woo Cho, Junghyun Park, Seung-Yeol Lee, Hwi Kim, and Byoungho Lee, Coupling of spin and angular momentum of light in plasmonic vortex, Opt. Express **20**, 10083 (2012).

[4] H. Su, X. Shen, G. Su, L. Li, J. Ding, F. Liu, P. Zhan, Y. Liu, and Z. Wang, Efficient generation of microwave plasmonic vortices via a single deep-subwavelength meta-particle, Laser Photonics Rev. **12**, 1800010 (2018).

[5] A. Berzanskis, A. Matijosius, A. Piskarskas, V. Smilgevicius, and A. Stabinis, Conversion of topological charge of optical vortices in a parametric frequency converter, Opt. Commun. **140**, 273 (1997).

[6] J. Zeng, L. Li, X. Yang, and J. Gao, Generating and separating twisted light by gradient-rotation split-ring antenna metasurfaces, Nano Lett. **16**, 3101 (2016).

[7] H. He, M. E. J. Friese, N. R. Heckenberg, and H. Rubinsztein-Dunlop, Direct observation of transfer of angular momentum to absorptive particles from a laser beam with a phase singularity, Phys. Rev. Lett. **75**, 826 (1995).

[8] D. G. Grier, A revolution in optical manipulation, Nature **424**, 810 (2003).

[9] S. Fürhapter, A. Jesacher, S. Bernet, and M. Ritsch-Marte, Spiral phase contrast imaging in microscopy, Opt. Express **13**, 689 (2005).

[10] R. Fickler, G. Campbell, B. Buchler, P. K. Lam, and A. Zeilinger, Quantum entanglement of angular momentum states with quantum numbers up to 10,010, Proc. Natl. Acad. Sci. U. S. A. **113**, 13642 (2016).

[11] T. Stav, A. Faerman, E. Maguid, D. Oren, V. Kleiner, E. Hasman, and M. Segev, Quantum entanglement of the spin

and orbital angular momentum of photons using metamaterials, Science **361**, 1101 (2018).

[12] G. Gibson, J. Courtial, M. J. Padgett, M. Vasnetsov, V. Pas'ko, S. M. Barnett, and S. Franke-Arnold, Free-space information transfer using light beams carrying orbital angular momentum, Opt. Express **12**, 5448 (2004).

[13] J. Wang, J.-Y. Yang, I. M. Fazal, N. Ahmed, Y. Yan, H. Huang, Y. Ren, Y. Yue, S. Dolinar, M. Tur, and A. E. Willner, Terabit free-space data transmission employing orbital angular momentum multiplexing, Nat. Photonics **6**, 488 (2012).

[14] H. Huang, G. Xie, Y. Yan, N. Ahmed, Y. Ren, Y. Yue, D. Rogawski, M. J. Willner, B. I. Erkmen, K. M. Birnbaum, S. J. Dolinar, M. P. J. Lavery, M. J. Padgett, M. Tur, and A. E. Willner, 100 Tbit/s free-space data link enabled by three-dimensional multiplexing of orbital angular momentum, polarization, and wavelength, Opt. Lett. **39**, 197 (2014).

[15] H. Ahmed, H. Kim, Y. Zhang, Y. Intaravanne, J. Jang, J. Rho, S. Chen, and X. Chen, Optical metasurfaces for generating and manipulating optical vortex beams, Nanophotonics **11**, 941 (2022).

[16] C. Brunet, P. Vaity, Y. Messaddeq, S. LaRochelle, and L. A. Rusch, Design, fabrication and validation of an OAM fiber supporting 36 states, Opt. Express **22**, 26117 (2014).

[17] G. Vallone, V. D'Ambrosio, A. Sponselli, S. Slussarenko, L. Marrucci, F. Sciarrino, and P. Villoresi, Free-space quantum key distribution by rotation-invariant twisted photons, Phys. Rev. Lett. **113**, 060503 (2014).

[18] Z. Wan, Y. Shen, Z. Wang, Z. Shi, Q. Liu, and X. Fu, Divergence-degenerate spatial multiplexing towards future ultrahigh capacity, low error-rate optical communications, Light: Sci. Appl. **11**, 144 (2022).

[19] F. Gori, G. Guattari, and C. Padovani, Bessel-Gauss beams, Opt. Commun. **64**, 491 (1987).

[20] A. S. Ostrovsky, C. Rickenstorff-Parrao, and V. M. Arrizon, Generation of the "perfect" optical vortex using a liquid-crystal spatial light modulator, Opt. Lett. **38**, 534 (2013).

[21] Shiyao Fu and Chunqing Gao, Selective generation of arbitrary vectorial vortex beams, Acta Opt. Sin. **39**, 0126014 (2019).

[22] M. Berry, Making waves in physics, Nature **403**, 21 (2000).

[23] B. J. McMorran, A. Agrawal, I. M. Anderson, A. A. Herzing, H. J. Lezec, J. J. McClelland, and J. Unguris, Electron vortex beams with high quanta of orbital angular momentum, Science **331**, 192 (2011).

[24] G. C. G. Berkhout, M. P. J. Lavery, J. Courtial, M. W. Beijersbergen, and M. J. Padgett, Efficient sorting of orbital angular momentum states of light, Phys. Rev. Lett. **105**, 153601 (2010).

[25] N. Yu, P. Genevet, M. A. Kats, F. Aieta, J.-P. Tetienne, F. Capasso, and Z. Gaburro, Light propagation with phase discontinuities: Generalized laws of reflection and refraction, Science **334**, 333 (2011).

[26] X. Cai, J. Wang, M. J. Strain, B. Johnson-Morris, J. Zhu, M. Sorel, J. L. O'Brien, M. G. Thompson, and S. Yu, Integrated compact optical vortex beam emitters, Science **338**, 363 (2012).

[27] Z. Zhang, X. Qiao, B. Midya, K. Liu, J. Sun, T. Wu, W. Liu, R. Agarwal, J. M. Jornet, S. Longhi, N. M. Litchinitser, and L. Feng, Tunable topological charge vortex microlaser, Science **368**, 760 (2020).

[28] C. Paterson, Atmospheric turbulence and orbital angular momentum of single photons for optical communication, Phys. Rev. Lett. **94**, 153901 (2005).

[29] J. B. Pendry, D. Schurig, and D. R. Smith, Controlling electromagnetic fields, Science **312**, 1780 (2006).

[30] U. Leonhardt, Optical conformal mapping, Science **312**, 1777 (2006).

[31] D. Schurig, J. J. Mock, B. J. Justice, S. A. Cummer, J. B. Pendry, A. F. Starr, and D. R. Smith, Metamaterial electromagnetic cloak at microwave frequencies, Science **314**, 977 (2006).

[32] H. Chen and C. T. Chan, Transformation media that rotate electromagnetic fields, Appl. Phys. Lett. **90**, 241105 (2007).

[33] M. Rahm, D. Schurig, D. A. Roberts, S. A. Cummer, D. R. Smith, and J. B. Pendry, Design of electromagnetic cloaks and concentrators using form-invariant coordinate transformations of Maxwell's equations, Photonics Nanostruct. Fundam. Appl. **6**, 87 (2008).

[34] S. Firuzi and S. Gong, Long-range optical pulling force device based on vortex beams and transformation optics, J. Opt. **21**, 065401 (2019).

[35] J. Yi, Z. Shi, D. Li, C. Liu, H. Sun, L. Zhu, X. Chen, and S. N. Burokur, A metamaterial lens based on transformation optics for horizontal radiation of OAM vortex waves, J. Appl. Phys. **129**, 104101 (2021).

[36] L. Xiang and Z. Zhan, in *2017 IEEE International Symposium on Antennas and Propagation & USNC/URSI National Radio Science Meeting* (2017), pp. 1269–1270.

[37] R. Feng, J. Yi, S. N. Burokur, L. Kang, H. Zhang, and D. H. Werner, Orbital angular momentum generation method based on transformation electromagnetics, Opt. Express **26**, 11708 (2018).

[38] Y. Lai, W. Dong, and J. Hu, Generation of various vortex beams based on transformation materials, J. Opt. **25**, 035702 (2023).

[39] J. Liao, P. Zhao, Z. Zhang, W. Xiao, and H. Chen, Mirrored transformation optics, Opt. Lett. **49**, 907 (2024).

[40] D. Schurig, J. B. Pendry, and D. R. Smith, Calculation of material properties and ray tracing in transformation media, Opt. Express **14**, 9794 (2006).

[41] M. V. Berry, A note on superoscillations associated with Bessel beams, J. Opt. **15**, 044006 (2013).

[42] Q. Duan, Y. Yin, L. Han, S. Zhu, Y. Zhou, H. R. Chen, and H. Chen, Observation of vortex Hall effect in double negative index materials, Adv. Opt. Mater. **11**, 2202111 (2023).

[43] Y. Fu, Y. Xu, H. Chen, and S. A. Cummer, Coherent perfect absorption and laser modes in a cylindrical structure of conjugate metamaterials, New J. Phys. **20**, 013015 (2018).

[44] Y. Yin, Q. Duan, J. Li, C. Qiu, and H. Chen, Evolution of optical vortices in gradient media and curved spaces, Opt. Lett. **48**, 315 (2023).

[45] R. Liu, C. Ji, J. J. Mock, J. Y. Chin, T. J. Cui, and D. R. Smith, Broadband ground-plane cloak, Science **323**, 366 (2009).

[46] R. Liu, Q. Cheng, J. Y. Chin, J. J. Mock, T. J. Cui, and D. R. Smith, Broadband gradient index microwave quasi-optical elements based on non-resonant metamaterials, Opt. Express **17**, 21030 (2009).

[47] K.-P. Ye, W.-J. Pei, Z.-H. Sa, H. Chen, and R.-X. Wu, Invisible gateway by superscattering effect of metamaterials, Phys. Rev. Lett. **126**, 227403 (2021).

[48] S. A. Cummer, B.-I. Popa, D. Schurig, D. R. Smith, and J. Pendry, Full-wave simulations of electromagnetic cloaking structures, Phys. Rev. E **74**, 036621 (2006).

[49] F. Sun, Y. Liu, S. Zhong, and S. Zhang, Editorial: Transformation optics and its frontier branches, Front. Mater. **10**, 1310326 (2023)..

[50] L. Xu and H. Chen, Transformation metamaterials, Adv. Mater. **33**, 2005489 (2021).

[51] X. Jiang, N. Wang, C. Zhang, X. Fang, S. Li, X. Sun, Y. Li, D. Ta, and W. Wang, Acoustic orbital angular momentum prism for efficient vortex perception, Appl. Phys. Lett. **118**, 071901 (2021).